AGU PUBLICATIONS

JGR

Journal of Geophysical Research: Atmospheres

RESEARCH ARTICLE
10.1002/2016JD024753

Key Points:
- A new strategy is proposed to analyze convective and large-scale mass fluxes from satellite data
- The systematic evolution of the mass fluxes is captured in association with convective development
- The findings have the potential to serve as an observational basis to assess GCM parameterizations

Correspondence to:
H. Masunaga,
masunaga@nagoya-u.jp

Citation:
Masunaga, H., and Z. J. Luo (2016), Convective and large-scale mass flux profiles over tropical oceans determined from synergistic analysis of a suite of satellite observations, *J. Geophys. Res. Atmos.*, *121*, doi:10.1002/2016JD024753.

Received 22 FEB 2016
Accepted 16 JUN 2016
Accepted article online 24 JUN 2016

Convective and large-scale mass flux profiles over tropical oceans determined from synergistic analysis of a suite of satellite observations

Hirohiko Masunaga[1] and Zhengzhao Johnny Luo[2]

[1]Institute for Space-Earth Environmental Research, Nagoya University, Nagoya, Japan, [2]Department of Earth and Atmospheric Sciences and NOAA-CREST Institute, City University of New York, City College, New York, New York, USA

Abstract A new, satellite-based methodology is developed to evaluate convective mass flux and large-scale total mass flux. To derive the convective mass flux, candidate profiles of in-cloud vertical velocity are first constructed with a simple plume model under the constraint of ambient sounding and then narrowed down to the solution that matches satellite-derived cloud top buoyancy. Meanwhile, the large-scale total mass flux is provided separately from satellite soundings by a method developed previously. All satellite snapshots are sorted into a composite time series that delineates the evolution of a vigorous and organized convective system. Principal findings are the following. First, convective mass flux is modulated primarily by convective cloud cover, with the intensity of individual convection being less variable over time. Second, convective mass flux dominates the total mass flux only during the early hours of the convective evolution; as convective system matures, a residual mass flux builds up in the mass flux balance that is reminiscent of stratiform dynamics. The method developed in this study is expected to be of unique utility for future observational diagnosis of tropical convective dynamics and for evaluation of global climate model cumulus parameterizations in a global sense.

1. Introduction

Moist convection has been long known to be a critical element of the tropical atmospheric circulations. It remains an elusive problem, however, to thoroughly formulate the convective processes in light of large-scale dynamics, despite of a series of achievements since early monumental work, for instance, by *Yanai et al.* [1973] and *Arakawa and Schubert* [1974]. It is noted that "large scale" refers here to a horizontal scale of O(100) km, comparable to the typical grid size of traditional climate models. A challenge remains partly, if not largely, because global observations to verify theories and numerical models are not readily available. Although efforts have been made over decades to observe convective and ambient air mass fluxes by various means including aircraft wind measurements [*LeMone and Zipser*, 1980] and more recently by wind profilers [e.g., *May and Rajopathyaya*, 1999; *Kumar et al.*, 2015], the spatial and temporal sampling is often so limited that it is difficult to physically interpret those measurements in a robust large-scale context to generalize the findings. Long-term, global observations from satellites could offer a solution to the sampling problem. However, no satellite instrument currently in orbit is designed for the purpose of measuring vertical velocity at any spatial scale. A new approach is explored in this study to work out this difficulty, by combining and extending two satellite-based analysis methods recently developed by the authors so that both large-scale and convective-scale mass fluxes are estimated over the globe.

The first method was developed to target convective plumes sampled by CloudSat and other A-Train measurements. It produces estimates of cloud top buoyancy [*Luo et al.*, 2010] and cloud top vertical velocity [*Luo et al.*, 2014] at convective scale on the order of 1 km (O(1 km)). These two estimates, in particular the cloud top buoyancy, are adopted in the current study to derive convective mass fluxes (section 2.2). The second method of interest was proposed by *Masunaga and L'Ecuyer* [2014], where large-scale (O(100 km)) vertical motion is quantified from a thermodynamic budget analysis applied to infrared soundings and other satellite measurements. These two independent techniques in tandem provide a unique opportunity to study jointly the convective mass flux and total large-scale mass flux, the latter of which formally includes downdraft mass flux as well. These two mass flux estimates from the present techniques are, although subject to their own uncertainties, by design free of any external assumption prescribing the physical linkage between

Table 1. Summary of Satellite Data Analyzed in This Work

Platforms	Instruments	Description	Footprint Size	Target Parameters
TRMM	PR	Ku-band radar	4.3 km at nadir	Convective occurrence for the composite base point
Aqua	AIRS	Hyperspectral IR sounder	13.5 km at nadir	Air temperature and water vapor profiles
Aqua	AMSR-E	Microwave radiometer	74 km × 43 km to 6 km × 4 km	SST, CWV, and surface precipitation
Aqua	MODIS	Vis/IR imager	1 km at nadir	Cloud top temperature
CloudSat	CPR	W band radar	1.7 km × 1.3 km	Cloud top height, cumulus occurrence, and Q_R
CALIPSO	CALIOP	Lidar	100 m	Cloud top height
QuikSCAT	SeaWinds	Microwave scatterometer	37 km × 25 km	Wind at 10 m height

convective clouds and their environment. In general circulation models (GCMs), the total large-scale mass flux is explicitly simulated in a prognostic manner, whereas the convective mass flux is treated implicitly in cumulus parameterization. Findings from our study will thus serve as an important observational basis against which GCM cumulus parameterization, or more generally the interaction between convection and large-scale environment, may be vigorously evaluated. This article, as the first of a series of papers to follow, is intended to report the proposed methodology and some preliminary results applied to observations over tropical oceans, leaving in-depth analysis and specific applications for future work.

A summary of the input satellite data and a review of the methods from those previous papers are presented in section 2. A simple plume model is described in section 3.1 to construct the in-cloud vertical velocity profiles that are matched with cloud top buoyancy and vertical velocity estimates (section 3.2). The analysis results for 2 years (2008–2009) are presented in section 4, followed by discussions and summary in section 5. A brief error analysis is provided in Appendix A.

2. Satellite Data, Derived Parameters, and Composite Method

This section is devoted to a brief summary of the data and method from previous studies employed as an input to the present analysis. Further technical details are found in the cited references.

2.1. Data Summary

The satellite instruments used in this study are summarized in Table 1. The Tropical Rainfall Measuring Mission (TRMM) Precipitation Radar (PR) offers a reliable measure of precipitation (or rain-cell) occurrence and is used as the "anchor" of statistical time series before and after convection is developed (to be detailed in section 2.4). The Atmospheric Infrared Sounder and Advanced Microwave Sounder Unit (AIRS/AMSU, hereafter AIRS collectively) Level-2 product provides the vertical profiles of temperature and humidity at a vertical resolution of roughly 1 km [*Susskind et al.*, 2003, 2011]. Column water vapor (CWV) and sea surface temperature (SST) are obtained from the Advanced Microwave Scanning Radiometer for Earth Observing System (AMSR-E) data sets produced by the Remote Sensing Systems [*Wentz and Meissner*, 2000]. AMSR-E is employed also for surface precipitation estimates with the Goddard Profiling (GPROF) 2010 data [*Kummerow et al.*, 2011]. Ocean surface wind estimates are taken from the Quick Scatterometer (QuikSCAT) SeaWinds Level-3 daily gridded data set [*Perry*, 2001]. The CloudSat Cloud Profiling Radar (CPR) and the Cloud-Aerosol Lidar and Infrared Pathfinder Satellite Observation (CALIPSO) Cloud-Aerosol Lidar with Orthogonal Polarization (CALIOP) are utilized for determining the cloud top height of convective clouds, while cloud top temperature is estimated from the Moderate Resolution Imaging Spectroradiometer (MODIS). The footprint size varies on an instantaneous basis from sensor to sensor, but the inconsistency in spatial resolution is alleviated when the estimates are averaged over a large-scale (100 km radius) domain in the present analysis.

Pressure levels are fixed at 925, 850, 700, 600, 500, 400, 300, 250, 200, 150, and 100 hPa in accordance with the AIRS product design. Additional two levels below 925 hPa are introduced to represent the surface and cloud base, the latter of which is given by the lifting condensation level determined with the near-surface temperature and humidity estimates from the AIRS observations.

2.2. Cloud Top Buoyancy and Vertical Velocity

Cloud top buoyancy of convective clouds is derived based on the normalized temperature difference between the cloud top and the ambient air at the same height [*Luo et al.*, 2010; *Takahashi and Luo*, 2012; *Wang et al.*, 2014]. Cloud top temperature is evaluated with IR measurements from MODIS, with an IR emissivity correction

applied making use of simultaneous observations from the CALIPSO and CloudSat satellites. CloudSat radar echoes are used also for determining cloud top height and ensuring that a detected convective core continuously extends up from the cloud base located near the surface. It is noted that the cases where near-surface echoes disappear due to heavy attenuation by precipitation are assumed to be associated with vigorous convection and are retained in the samples. The ambient temperature is adopted from the collocated European Centre for Medium-Range Weather Forecast (ECMWF) operational analysis. A key observational requirement for buoyancy estimation is simultaneous and independent measurements of cloud top height (CloudSat) and cloud top temperature (MODIS), as well as information on ambient temperature profile (ECMWF).

Shallow convection is, in general, difficult to capture with a sufficient level of confidence in the present methodology, so cloud top buoyancy and vertical velocity estimates are unavailable where cloud top is lower than 3 km. This criterion imposes a major restriction on sampling completeness, given the prevalence of shallow cumuli over tropical oceans [*Johnson et al.*, 1999; *Short and Nakamura*, 2000]. The current analysis tentatively deals with shallow cumuli in a simplified approach as described later in section 4, leaving a more realistic treatment for follow-up work in the future. It is hence stressed that the primary interests of the present work are confined to deep convection and congestus.

Buoyancy is in theory affected by in-cloud and ambient humidity (through the virtual temperature effect) and the condensate loading in addition to the temperature difference (see (12) in section 3.1). The effects of humidity and condensate are not considered in the current measure of cloud top buoyancy in order to avoid unnecessary complication. This is deemed to be justifiable since we focus mainly on deep convection and congestus where cloud top temperatures are low enough such that the vapor and condensate mixing ratios are generally very small.

Luo et al. [2014] demonstrated that convective cloud top vertical velocity can be evaluated by exploiting a small overpass time difference between the two IR sensors belonging to the A-Train constellation, namely, the Aqua MODIS and the CALIPSO Imaging Infrared Radiometer (IIR). Basically, an actively developing convective plume will grow colder with time, and its cloud top vertical velocity is proportional to the change rate of cloud top temperature with time. By measuring the time-differenced cloud top temperature, together with knowledge of the lapse rate, one can estimate the convective cloud top vertical velocity. We have used both cloud top vertical velocity and cloud top buoyancy in our analysis and found the results were virtually the same. Although cloud top vertical velocity may appear as a more natural choice for deriving the whole in-cloud profile of vertical velocity than using cloud top buoyancy, the observational requirements are far more restrictive for the former. Hence, there are significantly more data points for buoyancy than for vertical velocity, leading to a less noisy analysis result. This paper, therefore, presents only the buoyancy-based analysis.

2.3. Large-Scale Vertical Motion

The vertical profiles of humidity and temperature observed from the AIRS serve as a primary input into the moisture and thermal budget analysis that is employed for evaluating large-scale vertical p velocity, $\overline{\omega}$, or equivalently the total large-scale mean mass flux, $\overline{M_0}$, multiplied by gravitational acceleration.

The moisture and thermal budget equations integrated vertically over the troposphere serve as diagnostic formulae to evaluate moisture convergence and dry static energy (DSE) convergence, given the other terms all constrained observationally

$$-\langle\overline{\nabla\cdot q\mathbf{v}}\rangle = \frac{\partial}{\partial t}\langle q\rangle - \overline{E} + \overline{P} \tag{1}$$

and

$$-\langle\overline{\nabla\cdot s\mathbf{v}}\rangle = \frac{\partial}{\partial t}\langle s\rangle - \overline{S} - L_v\overline{P} - \langle Q_R\rangle, \tag{2}$$

where $\langle\cdots\rangle$ denotes the vertical integral over the troposphere, q the vapor mixing ratio, s the DSE, $\mathbf{v}$ the horizontal wind, E the evaporative flux, P the surface precipitation, S the sensible heat flux, L_v the specific latent heat of vaporization, and Q_R the radiative heating rate. The overbar designates horizontal averaging over a large-scale domain with the radius of 100 km.

The moisture and DSE convergence integrated vertically may be viewed as lower and upper troposphere weighted convergence, respectively, because moisture has higher concentration in the lower troposphere while DSE has greater value in the upper troposphere. Vertical velocity, or the vertical integral of horizontal convergence, may be therefore obtained in each lower and upper troposphere exploiting (1) and (2),

respectively, together. This idea is further extended so that a complete vertical profile of $\overline{\omega}$ is obtained when the degree of freedom is reduced to a tractable level through vertical mode decomposition into the first and second baroclinic modes and the shallow mode combined with a time-invariant background state of $\overline{\omega}$. The equations to yield the three ω modes consist of

$$\sum_i \left\langle q \frac{\partial \overline{\omega}_i}{\partial p} \right\rangle \approx -\langle \overline{\nabla \cdot q\mathbf{v}} \rangle, \tag{3}$$

$$\sum_i \left\langle s \frac{\partial \overline{\omega}_i}{\partial p} \right\rangle \approx -\langle \overline{\nabla \cdot s\mathbf{v}} \rangle, \tag{4}$$

where the subscript *i* represents each vertical mode, and

$$\sum_i \overline{\omega}_{i,\mathrm{CB}} = \langle \overline{\nabla \cdot q\mathbf{v}} \rangle_{\mathrm{SC}}, \tag{5}$$

where $\overline{\omega}$ at cloud base (CB) is quantified from the subcloud layer (SC) convergence determined with QuikSCAT winds. The right-hand side of equations (3) and (4) are as given by equations (1) and (2). The sum of all the three modes, $\overline{\omega}_i$, yields $\overline{\omega}$ and serves as the total large-scale mass flux discussed in section (4). More details in methodology are provided by *Masunaga and L'Ecuyer* [2014].

2.4. Integration Into Composite Time Series

Cloud top buoyancy (and cloud top vertical velocity) and large-scale $\overline{\omega}$ retrievals are applied individually to instantaneous measurements over global tropical oceans. Convective cloud structure is substantially different over land from over ocean [*Liu et al.*, 2007], so aspects of the current findings apply only to oceanic convective systems. Limiting the analysis to oceans mitigates the diurnal sampling bias in Sun-synchronous satellite measurements owing to the weakness of diurnal variation in oceanic precipitation [e.g., *Imaoka and Spencer*, 2000]. The observations are time stamped according to the temporal difference with respect to the time when the TRMM PR detects rain cells some hours before or after at the same location and are then averaged over the surrounding 100 km radius domain for each hour to constitute a composite time sequence around the time of rain cell occurrence (*Masunaga* [2012], see the schematic in Figure 1). Note that this circular domain is comparable in area to a 177 km × 177 km box if applied to a square field.

The number of A-Train buoyancy samples ranges from about 3000 to 6000 for each hourly bin in composite space, as shown later in section 4 and Figure 6c. The AIRS samples for large-scale $\overline{\omega}$ consist of roughly 30,000–300,000 each hour, for which the minimum corresponds to the hours of peak convection because infrared sounding is unavailable for totally cloudy skies. The composite time series shown in this work are hence constructed with a reasonably large body of statistics. The robustness of the composite statistics, including the potential errors due to the migration of convective disturbances, has been assessed in *Masunaga* [2015].

The TRMM detection of rain cells is defined when the PR finds precipitation echoes beyond the noise level across a few vertically consecutive bins within a column, flagged as the "rain certain" in the TRMM data product. In the present analysis, this procedure is carried out only when the TRMM PR finds the rain cell coverage exceed 50% of the 100 km radius domain. As such, the resulting time series is considered as a statistical representation of the variability over time in association with the development and dissipation of highly organized convective systems (see Figure 2 of *Masunaga* [2013]). The present compositing procedure has another advantage that the composite 100 km domain contains a large number of CloudSat/CALIPSO samples as noted above, although those samples, confined spatially to a narrow vertical scan, cover only a fraction of the domain on an instantaneous basis.

The QuikSCAT satellite had the Sun-synchronous orbit of ~6:00 local time, flying behind the A-Train satellites by roughly 4.5 h. This temporal offset could potentially introduce some bias when the QuikSCAT and A-Train measurements are combined into the composite time series. The bias would be, however, small because the diurnal cycle of tropical disturbances is modest as mentioned above, with the magnitude being not larger than 30% in surface divergence over tropical oceans [*Deser*, 1994]. This magnitude should be further reduced when the opposite diurnal phases are averaged between ascending and descending orbits.

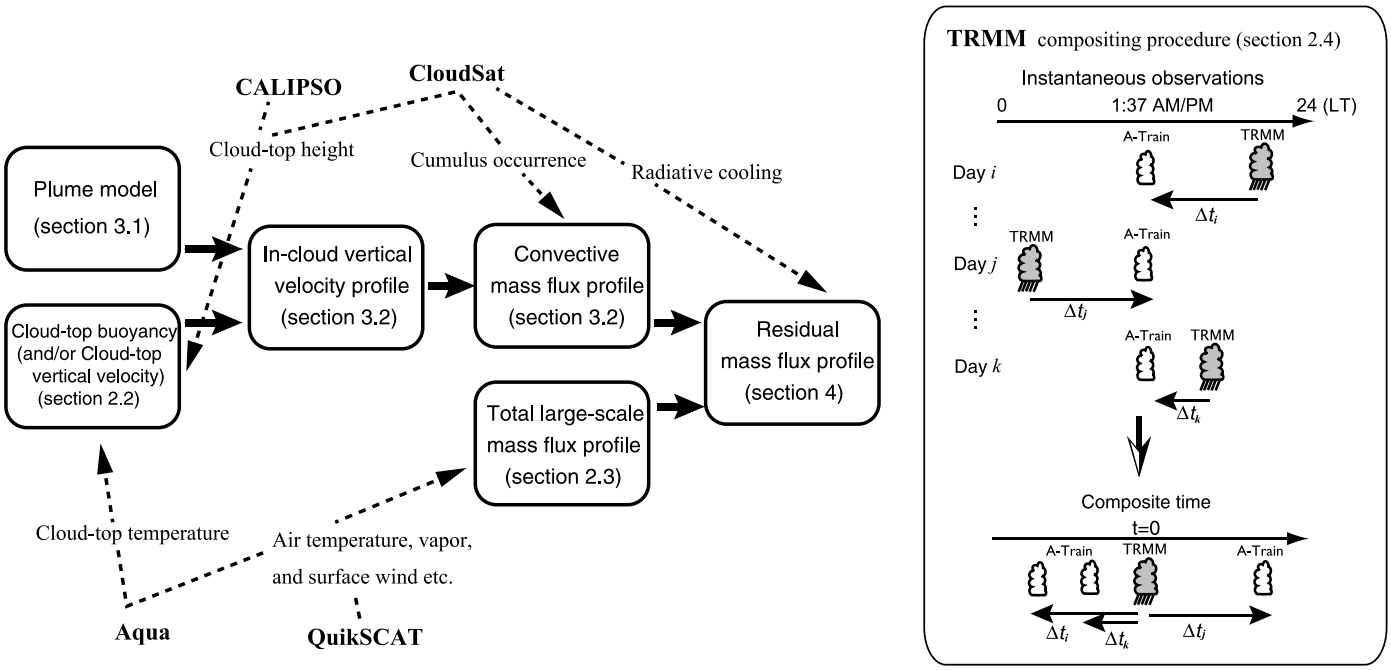

Figure 1. Flowchart of the analysis procedures. Solid arrows indicate the analysis flow and dashed arrows represent the primary input parameters and the satellites that provide these parameters. The schematic on the right shows the current composite technique where many pairs of TRMM and A-Train snapshots are averaged into statistical time series. Here the A-Train snapshots consist of the parameters as shown in each flowchart box except for the "plume model," while the TRMM is employed to seek the occurrence of rain cells that may be prior or subsequent to each A-Train snapshot (see section 2.4 for details).

2.5. Analysis Period and Area

The analysis period spans 2 years from 1 January 2008 to 31 December 2009 for cloud top buoyancy estimates (section 2.2). The large-scale vertical motion (section 2.3) is constructed with a longer period from 1 December 2002 to 30 November 2009 to ensure the statistical robustness in the composite time series (section 2.4). The difference in the temporal length is not essential since the composite statistics are known to be insensitive to the choice of the analysis period [*Masunaga*, 2015].

The target region is global tropical oceans between 15°S and 15°N with land masses all excluded. Tropical clouds, in particular organized convective systems, are known to be distributed nonuniformly over tropical oceans [e.g., *Mohr and Zipser*, 1996]. However, our previous results (e.g., Figure 12 of *Masunaga* [2013]) show that the overall features of the sampled convective systems, conditioned on the 50+% coverage as defined above, are insensitive to the regionality such as the east versus west Pacific. The statistics are in effect representative of convective active regions in general. It follows that individual systems selected by the common criteria exhibit certain universal characteristics beyond the climatological differences in their large-scale environment.

3. In-cloud Vertical Velocity Profiles

Buoyancy or vertical velocity estimates from radar and IR measurements are available only at cloud tops, while the full in-cloud structure of updraft velocity is required for our science goal. A new strategy is developed in this work to reconstruct the in-cloud vertical velocity profiles with the aid of a steady state single-column plume model described in section 3.1. Entrainment rate, a key uncertainty in the model, is varied so that a broad range of solutions are allowed to exist for a given environmental sounding. A Bayesian procedure is then applied to narrow down the candidate profiles to the solution that best matches the cloud top buoyancy or vertical velocity estimates derived from observations (section 3.2). A flowchart is shown in Figure 1 to outline the whole procedures in the present work.

The plume model developed here is by design meant to represent updraft in cumulus convection without convective downdraft and mesoscale dynamics considered. This definition is consistent with the cloud top buoyancy and vertical velocity estimation from satellites, where the samples are conservatively chosen to focus on rapidly growing convective cores [*Luo et al.*, 2010, 2014], which belong, together with the

surrounding stratiform clouds, to the organized system identified by the TRMM during hours around zero. The present analysis, however, formally includes the downdrafts as well in terms of the residual in the large-scale mass flux balance as discussed later in section 5.

3.1. Single-Column Plume Model

The entrainment and detrainment rates, ϵ and δ, are defined conventionally as

$$\frac{1}{\rho w_c}\frac{\partial(\rho w_c)}{\partial z} = \epsilon - \delta, \tag{6}$$

where w is vertical velocity, ρ is the mass density of air, and the subscript c indicates in-cloud properties. The entrainment and detrainment rates may be separated into dynamic and turbulent components [*Houghton and Cramer*, 1951],

$$\epsilon = \epsilon_{\mathrm{dyn}} + \epsilon_{\mathrm{tur}}, \quad \delta = \delta_{\mathrm{dyn}} + \delta_{\mathrm{tur}}, \tag{7}$$

where the dynamic components are determined so as to satisfy the mass conservation [*Asai and Kasahara*, 1967]

$$\epsilon_{\mathrm{dyn}} = \frac{1}{\rho w_c}\frac{\partial(\rho w_c)}{\partial z} H\left[\frac{\partial(\rho w_c)}{\partial z}\right], \quad \delta_{\mathrm{dyn}} = -\frac{1}{\rho w_c}\frac{\partial(\rho w_c)}{\partial z} H\left[-\frac{\partial(\rho w_c)}{\partial z}\right], \tag{8}$$

where H is the Heaviside function. The turbulent components are by definition canceled out at each height in the continuity equation (i.e., $\epsilon_{\mathrm{tur}} = \delta_{\mathrm{tur}}$) while not eliminated in the other conservation equations described below.

The conservation of an arbitrary parameter φ may be written as

$$\frac{\partial(\rho w_c \varphi_c)}{\partial z} = \rho w_c(\epsilon\varphi_a - \delta\varphi_c) + \rho\sum_i F_{\varphi,i}, \tag{9}$$

where the subscript a designates the ambient environment and $F_{\varphi,i}$ accounts for the source and sink terms as needed. Equations (6) and (9) are combined into

$$\frac{\partial\varphi_c}{\partial z} = -\epsilon(\varphi_c - \varphi_a) + \frac{1}{w_c}\sum_i F_{\varphi,i}. \tag{10}$$

Note that the detrainment terms, although not explicitly apparent in (10), remain in the formulation as originally defined. The equation of motion is derived as

$$\frac{1}{2}\frac{\partial w_c^2}{\partial z} = a_B B - \epsilon w_c^2 - c_D w_c^2, \tag{11}$$

where φ has been replaced by w_c^2. Here the in-cloud buoyancy, B, is characterized by

$$B = g a_B\left(\frac{T_{v,c} - T_{v,a}}{T_{v,a}} - q_w\right), \tag{12}$$

where g is the gravitational acceleration and T_v is virtual temperature. The portion of the buoyancy production usable for vertical acceleration, a_B, is set to be 1/6 [*Gregory*, 2001]. The third term in the right-hand side of (11), aimed to account for a drag force owing to pressure perturbation from the hydrostatic state [e.g., *Simpson and Wiggert*, 1969], is highly uncertain and hence not explicitly specified here. Instead, uncertainties in c_D are formally combined into those in ϵ_{tur}. As such, ϵ_{tur} is the controlling parameter in this work to be chosen from a range of possibilities and then constrained by observations.

In-cloud moist static energy (MSE), h_c, is

$$h_c = c_p T_c + gz + L_v q_{v,c}, \tag{13}$$

where c_p is the specific heat capacity under constant pressure, and z is altitude. The conservation equation (10) is applied to the MSE budget with the freezing effect included (i.e., $\varphi_c = h_c - L_i q_i$ and $\varphi_a = h_a$),

$$\frac{\partial(h_c - L_i q_i)}{\partial z} = -\epsilon(h_c - L_i q_i - h_a), \tag{14}$$

where L_i is the specific latent heat of fusion and q_i is the ice mixing ratio. The ice mixing ratio is determined diagnostically as

$$q_i = f_i q_w, \quad \text{where } f_i = \frac{1 - \tanh[(T_c - T_{0,i})/dT_i]}{2} \tag{15}$$

where $T_{0,i}$ and dT_i are chosen to be −20°C and 7°C, respectively, so that f_i smoothly transitions from zero to unity as temperature decreases from 0°C to −40°C. In-cloud temperature T_c is obtained from h_c, assuming that the in-cloud air is saturated at all heights and $q_{v,c}$ is approximated by saturation vapor mixing ratio with respect to liquid water, $q_v^*(T_c)$. It has been confirmed that the buoyancy profiles remain similar when $q_v^*(T_c)$ is replaced by the saturation vapor pressure with respect to ice at cold temperatures.

Replacing φ_c with q_w in (10) leads to the equation for the condensate mixing ratio,

$$\frac{\partial q_w}{\partial z} = -\epsilon q_w + \frac{1}{w_c}(\dot{q}_{\text{cond}} - \dot{q}_{\text{auto}}), \tag{16}$$

where $\dot{q}_{\text{cond}}$ is the condensation rate and $\dot{q}_{\text{auto}}$ is the autoconversion rate. The ambient temperature and vapor profiles are known parameters taken from AIRS/AMSU soundings, same as those ingested for $\overline{\omega}$ estimates (section 2.3). The condensation rate is diagnosed from the vapor budget equation, obtained by substituting vapor mixing ratio q_v for φ in (10),

$$\dot{q}_{\text{cond}} = -w_c \left[\frac{\partial q_{v,c}}{\partial z} + \epsilon(q_{v,c} - q_{v,a}) \right]. \tag{17}$$

Here again $q_{v,c}$ is replaced by saturation vapor mixing ratio $q_v^*(T_c)$. The autoconversion rate is estimated using a primitive form of the Kessler formula [*Kessler*, 1969],

$$\dot{q}_{\text{auto}} = \frac{1}{\tau_{\text{auto}}}(q_w - q_{w,\text{crit}})H(q_w - q_{w,\text{crit}}), \tag{18}$$

where $\tau_{\text{auto}} = 10^3$ s and $q_{w,\text{crit}} = 10^{-3}$ kg kg^{-1}. Precipitating particles are assumed to immediately fall out of the ascending air, and their thermodynamic effects such as reevaporation and melting are not taken into account. The reader is reminded that the current plume model is designed to target convective updraft only.

Equations (11), (14), and (16) are integrated over height from cloud base to the level at which w_c reaches zero. Each vertical layer from the ambient soundings (see section 2.1) is divided into five sublayers for use by the numerical integration. The boundary condition for (14) and (16) is rather obvious: h_c is as observed from the satellite sounding, and q_w is zero immediately below cloud base. On the other hand, w_c at cloud base is not known from the observations and is assumed here to be twice as large as the subcloud layer vertical velocity scale, w_* (for further details, see *Grant* [2001] and *Gregory* [2001]). In this study, an approximate formula of w_* is adopted as

$$w_* \equiv \left(\frac{g z_{\text{CB}}}{\theta_{v,\text{SC}}} \overline{w'\theta'_{v0}} \right)^{1/3} \approx \left(\frac{g z_{\text{CB}}}{c_p T_{\text{SC}}} S \right)^{1/3}, \tag{19}$$

where T_{SC} and $\theta_{v,\text{SC}}$ are the temperature and virtual potential temperature averaged over the subcloud layer, z_{CB} is the cloud base height, $\overline{w'\theta'_{v0}}$ is the surface turbulent flux of virtual potential temperature, and S is surface sensible heat flux. The sensible heat flux is evaluated using a bulk formula as employed by *Masunaga* [2013]. Typical values of w_* estimated from the present satellite soundings are 0.6–0.7 m s^{-1}, which fall within the range studied by *Grant* [2001].

Figure 2 shows the plume model solutions for a range of ϵ_{tur} varied from 0 to 0.4 km^{-1}. The ambient soundings to force this run are taken from the composite time series at 24 h prior to the time of peak convection, but the results are qualitatively insensitive to the choice of timing. The normalized temperature difference, $(T_c - T_a)/T_a$, is presented as a proxy of buoyancy in Figure 2a, since this is the parameter to compare with cloud top observations in the Bayesian procedure described next (section 3.2). As expected, a change to the entrainment rate leads to a great difference in the depth of clouds from shallow cumulus topped near 700 hPa to overshooting deep convection reaching beyond 150 hPa. The resulting variation in the maximum updraft velocity spans a broad range from less than 3 m s^{-1} (shallow cumulus) to 14 m s^{-1} (deep convection) (Figure 2b). Shallow cumuli with even lower cloud tops are outside the present target and are not attempted

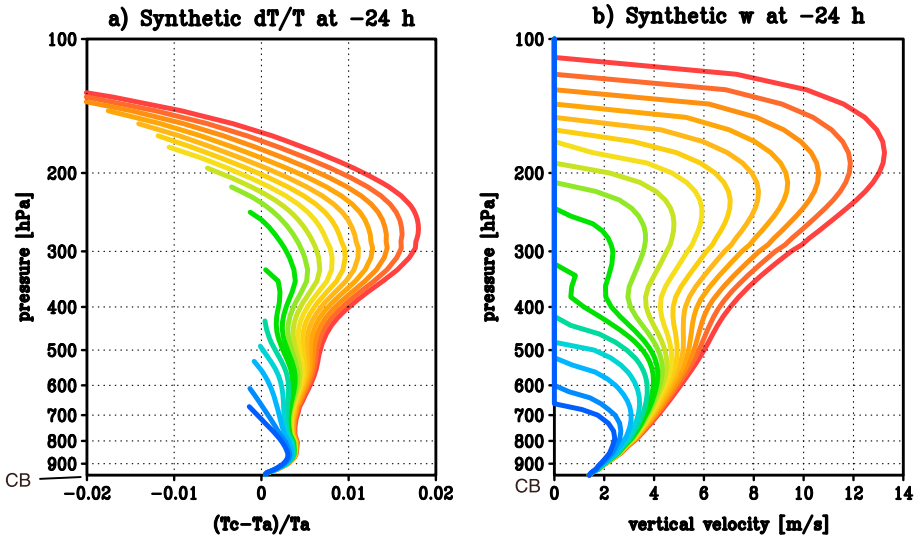

Figure 2. The plume model solutions of (a) $(T_c - T_a)/T_a$ and (b) w_c (m s^{-1}). Colors indicate different turbulent entrainment rates, ϵ_{tur}, changing by an increment of 0.01 km^{-1} from 0 up to 0.1 km^{-1}, followed by 0.12, 0.15, 0.2, 0.3, and 0.4 km^{-1} (from red to purple in the increasing order). The ambient soundings are taken from the composite time series at $t = -24$ h. Cloud base is labeled as "CB" on the pressure coordinate.

to simulate with the current model. The enhanced buoyancy above 400 hPa (Figure 2a) is brought by an additional heating owing to the freezing of cloud water, resulting in continuing acceleration of plumes as seen in the w_c profiles (Figure 2b). Vertical velocity then rapidly declines with height as buoyancy sharply drops to a large negative near the top of overshooting deep convection. The general characteristics of the w_c profiles simulated for deep convection is consistent with Doppler radar measurements by *Heymsfield et al.* [2010] in that w_c increases with height until it reaches the upper tropospheric peak exceeding 10 m s^{-1}.

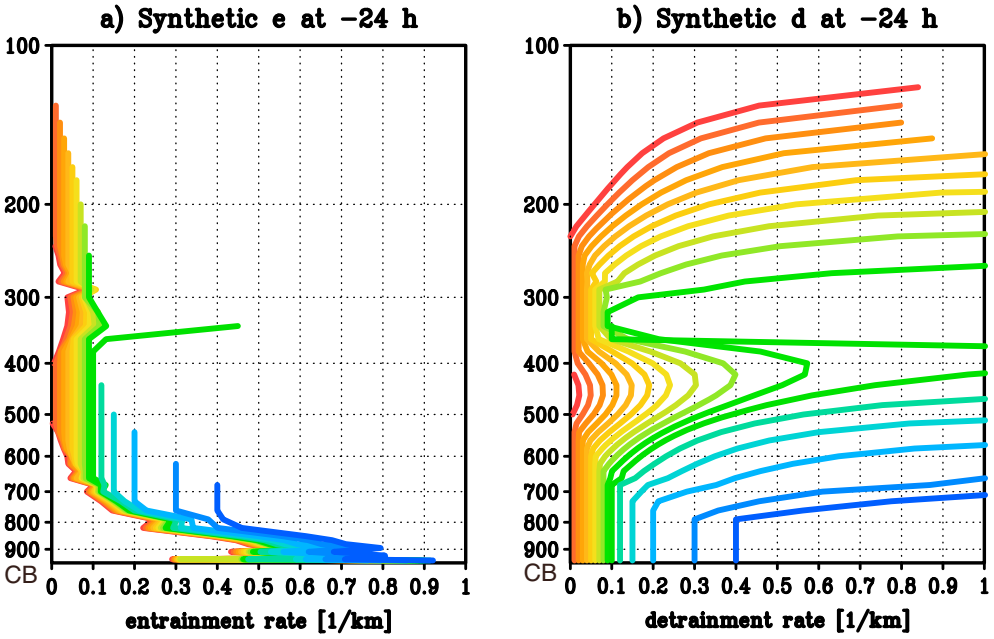

Figure 3. The plume model solutions of (a) the entrainment rate (km^{-1}), ϵ, and (b) the detrainment rate, δ (km^{-1}). Colors indicate different turbulent entrainment rates, ϵ_{tur}, changing by an increment of 0.01 km^{-1} from 0 up to 0.1 km^{-1}, followed by 0.12, 0.15, 0.2, 0.3, and 0.4 km^{-1} (from red to purple in the increasing order). The ambient soundings are taken from the composite time series at $t = -24$ h. Cloud base is labeled as "CB" on the pressure coordinate.

Table 2. Sensitivity Experiment Design for the Plume Model

Model Assumptions	Lower End	Control	Higher End
a_B	0.1	1/6 (0.166···)	0.2
dT_i	5 K	7 K	10 K
$q_{w,\mathrm{crit}}$	1×10^{-4} kg kg^{-1}	1×10^{-3} kg kg^{-1}	5×10^{-3} kg kg^{-1}
τ_{auto}	5×10^{2} s	1×10^{3} s	5×10^{3} s

The corresponding profiles of the entrainment and detrainment rates are shown in Figure 3. The overall vertical structure of ϵ is dominated by ϵ_{dyn} rather than ϵ_{tur}, the latter of which is assigned with a range of possible values constant over height. The entrainment rate is greatest immediately above cloud base, where the accelerating updraft efficiently sucks in the ambient air. The detrainment rate, with a somewhat larger spread depending on δ_{tur}, has a striking spike near cloud tops generated by an abrupt deceleration of updraft. Modest peaks at 400–500 hPa arise from the combination of a buoyancy loss by the condensate loading and the following recovery of buoyancy due to freezing. This midtropospheric detrainment peak is a factor responsible for the formation of cumulus congestus clouds prevailing over tropical oceans [*Johnson et al.*, 1999]. The idea that the effect of freezing on buoyancy could reinvigorate the updraft so the convective cloud eventually reaches the tropopause has been supported by later studies [e.g., *Zipser*, 2003] and will be worth revisiting in the future by recent satellite observations.

The simulated profiles presented above depend also on various model assumptions other than ϵ_{tur}. A set of sensitivity experiments are, therefore, conducted for assessing uncertainties in the assumptions. Each of a_B, dT_i, $q_{w,\mathrm{crit}}$, and τ_{auto} is perturbed one after another with all the other assumptions fixed at the control value. It is difficult to determine the realistic range of assumptions with confidence, so the lower and higher ends are chosen somewhat arbitrarily within roughly an order of magnitude as listed in Table 2. The results are presented in Figures 4 and 5. In all cases, the vertical profiles remain qualitatively similar in that w_c increases with height toward a single maximum, followed by a steep decline immediately above. A large spread in w_c arises for moderate entrainment rates (green shade) in Figure 5 because in these cases a subtle change to the assumptions could result in distinct consequences of either a buoyancy loss due to condensation loading (congestus) or a reinvigoration of updraft by freezing (deeper convection). Nevertheless, the spread due to any perturbation assumption (as represented by the breadth of the curves) is relatively small compared to the differences associated with varying ϵ_{tur} values, spanning across different curves from congestus to deep convection. It may be therefore concluded that ϵ_{tur} is the parameter responsible for yielding broad solutions from shallow cumulus to deep convection, while uncertainties in other assumptions per se are not so large as to entirely modify the depth of convection.

3.2. Synthesis of Satellite and Model Estimates

A set of the w_c profiles presented in the previous section (Figure 2b) constitutes a database to be searched for the optimal solution. The profile consistent with a given cloud top buoyancy (or cloud top vertical velocity) estimate is selected from the candidate solutions in a Bayesian manner [e.g., *Lorenc*, 1986]. The expectation of vertical velocity structure, $\hat{w}_c$, is

$$\hat{w}_c(z) \equiv \sum_i p(\epsilon_{\mathrm{tur},i}|z_T, \Delta T_T) w_{c,i}(z) = \sum_i p(\epsilon_{\mathrm{tur},i}) p(z_T, \Delta T_T|\epsilon_{\mathrm{tur},i}) w_{c,i}(z), \tag{20}$$

where $\epsilon_{\mathrm{tur},i}$ indicates the ith member of ϵ_{tur} (see the caption of Figure 2 for specific numbers), $w_{c,i}$ is the corresponding vertical velocity profile from the plume model, $p(\epsilon_{\mathrm{tur},i})$ is the priori probability distribution of $\epsilon_{\mathrm{tur},i}$, $p(\epsilon_{\mathrm{tur},i}|z_T, \Delta T)$ is the posteriori probability function for a given pair of observations of cloud top height, z_T, and the normalized temperature difference at the cloud top height, $\Delta T \equiv (T_c - T_a)/T_a$, and $p(z_T, \Delta T_T|\epsilon_{\mathrm{tur},i})$ is the conditional probability of z_T and ΔT for given ith plume model profile. The conditional probability distribution may be written as

$$p(z_T, \Delta T_T|\epsilon_{\mathrm{tur},i}) \propto \frac{1}{s_{0,i} - s_{\mathrm{CB}}} \int_{s_{\mathrm{CB}}}^{s_{0,i}} \exp\left[-\frac{(z_T - z_i(s))^2}{2\sigma_z^2} - \frac{(\Delta T_T - \Delta T_{c,i}(s))^2}{2\sigma_{\Delta T}^2} \right] \mathrm{d}s, \tag{21}$$

where σ_z and $\sigma_{\Delta T}$ are the measurement errors associated with z_T and ΔT, respectively. It is assumed in this work that σ_z =1 km and $\sigma_{\Delta T} \approx \sigma_T/T_a$ where σ_T = 1 K. The sensitivity to the choice of σ_z and $\sigma_{\Delta T}$ will be tested

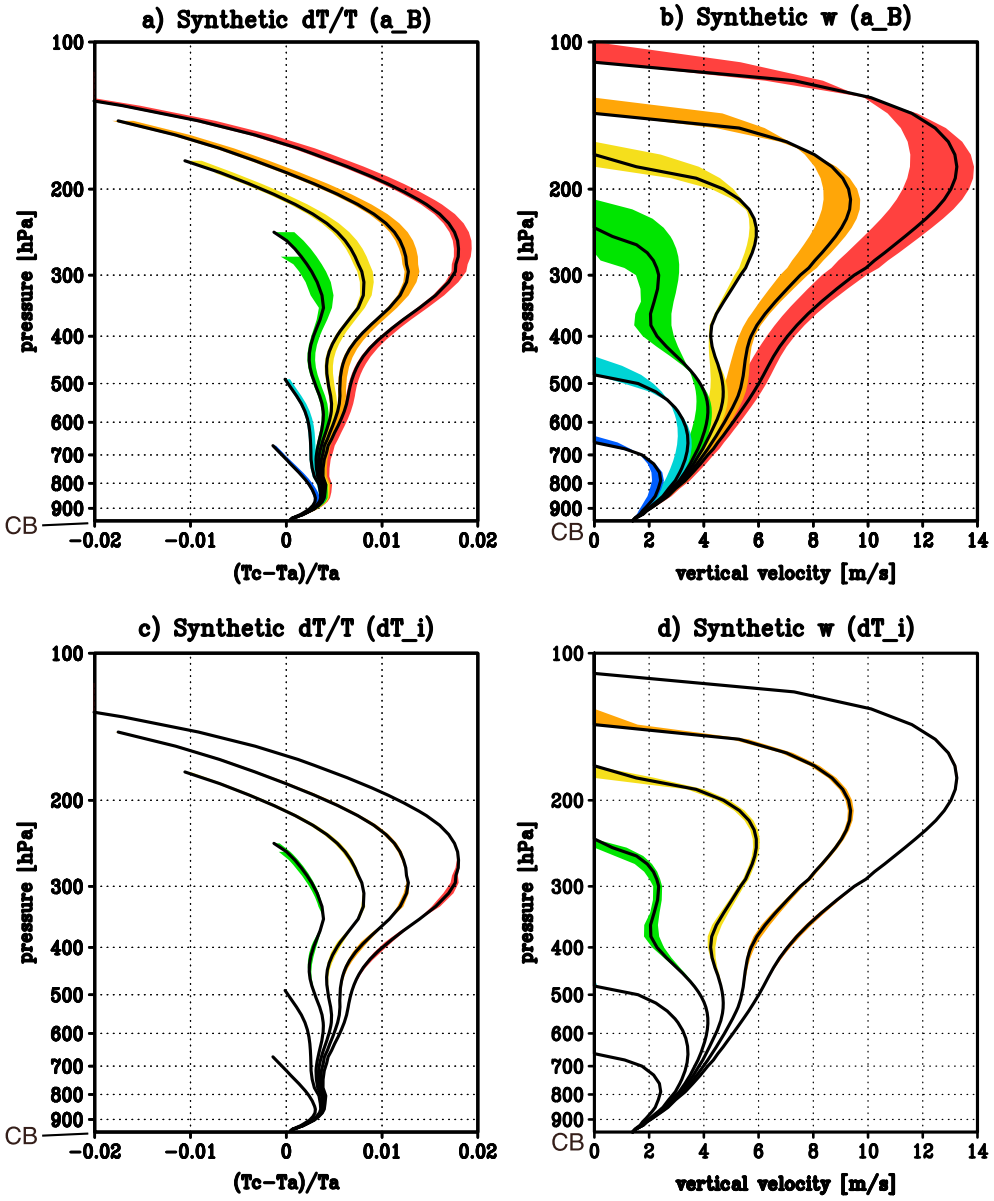

Figure 4. A sensitivity experiment of the plume model of (a and c) $(T_c - T_a)/T_a$ and (b and d) w_c (m s^{-1}) varying (a and b) a_B and (c and d) dT_i with all other assumptions fixed. Only every third profile (i.e., ϵ_{tur} =0, 0.03, 0.06, 0.09, 0.15, and 0.4 km^{-1}) for visual clarity. The resultant range of simulated profiles is color shaded around the control profile drawn in black. The ambient soundings are taken from the composite time series at $t = -24$ h. Cloud base is labeled as "CB" on the pressure coordinate.

in Appendix A. The integral is performed along the plume model trajectory, s, in the ΔT-z plane as drawn in Figure 2a from cloud base, s_{CB}, to the level at which w_c vanishes, $s_{0,i}$. The priori probability distribution $p(\epsilon_{\mathrm{tur},i})$ is initially assumed to be constant and is then updated by repeating the Bayesian procedure until the solution converges.

Mean convective intensity, $\overline{\hat{w}_c}$, and convective mass flux, $\overline{M_c}$, are each computed from $\hat{w}_c$ as

$$\overline{\hat{w}_c} = \frac{1}{A_w} \sum_{\in A_w} \hat{w}_c, \tag{22}$$

$$\overline{M_c} = \frac{1}{A_0} \sum_{\in A_w} \rho \hat{w}_c, \tag{23}$$

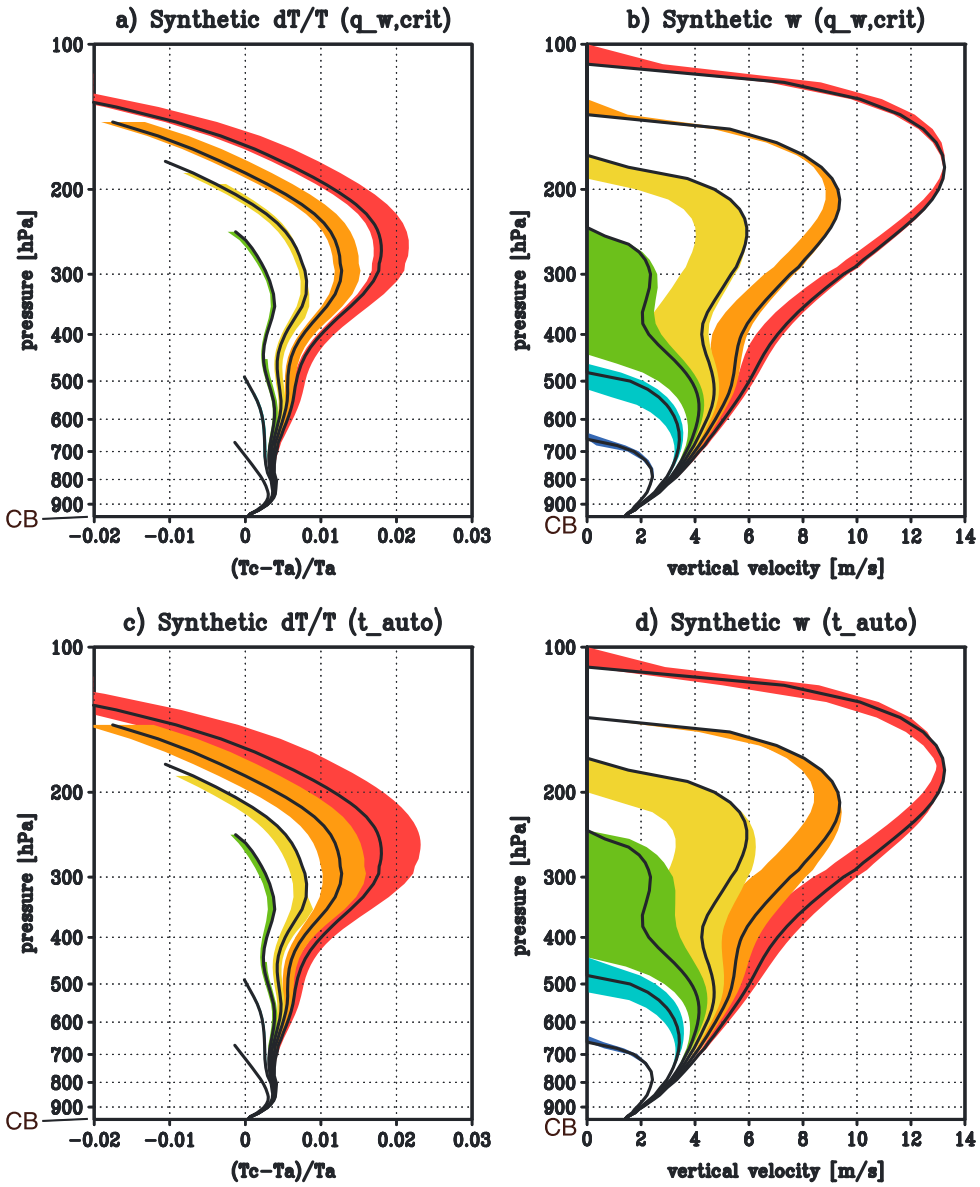

Figure 5. A sensitivity experiment of the plume model of (a and c) $(T_c - T_a)/T_a$ and (b and d) w_c (m s^{-1}) varying (a and b) $q_{w,\mathrm{crit}}$ and (c and d) τ_{auto} with all other assumptions fixed. Only every third profile (i.e., ϵ_{tur} =0, 0.03, 0.06, 0.09, 0.15, and 0.4 km^{-1}) for visual clarity. The resultant range of simulated profiles is color shaded around the control profile drawn in black. The ambient soundings are taken from the composite time series at $t = -24$ h. Cloud base is labeled as "CB" on the pressure coordinate.

where the area A_0 designates the portion of the large-scale domain that is sampled by CloudSat granules, and A_w denotes its subset constituted only of the footprints with nonzero buoyancy estimates, that is, the footprints where CloudSat detects deep convection and congestus. In (22) $\overline{\hat{w}_c}$ is averaged conditionally where convection is observed so that it provides a measure of convective intensity, while $\overline{M_c}$ in (23) is the unconditional mean over the whole large-scale domain, thus representing the convective mass flux as often used in GCM cumulus parameterizations.

4. The Composite Time Series of Vertical Velocity and Mass Flux

The analysis results from the algorithm outlined in section 3.2 are presented in this section. Potential errors associated with $\overline{M_c}$ are discussed later in Appendix A.

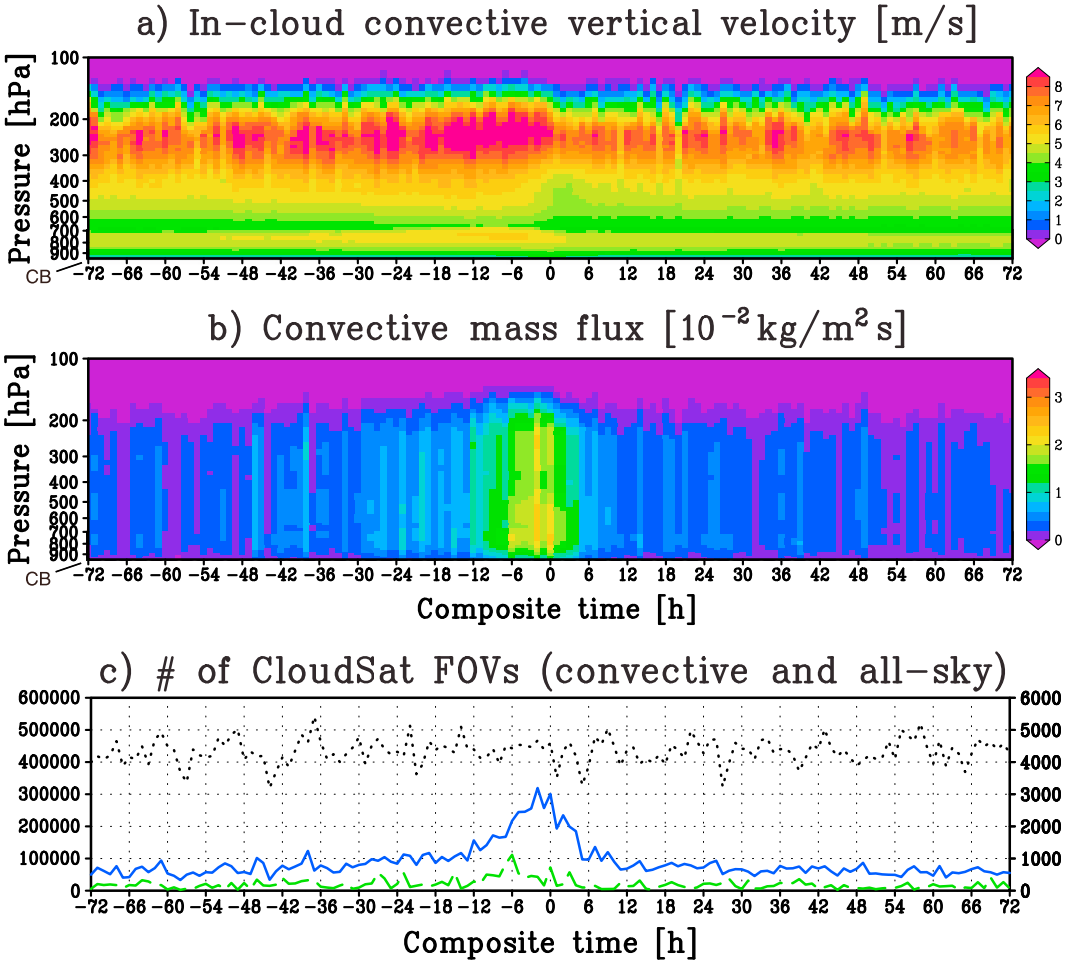

Figure 6. The composite time series of (a) vertical velocity $\overline{\hat{w}_c}$ (m s^{-1}), (b) convective mass flux $\overline{M_c}$ (10^{-2} kg m^{-2} s^{-1}), and (c) the number of hourly samples of all CloudSat footprints (black dotted, labeled on left), those with buoyancy estimates (blue solid, labeled on right), and shallow cumuli (green dashed, labeled on right). Cloud base is labeled as "CB" on the pressure coordinate. Altitudes lower than 3 km are hatched in (a) and (b) to mask out the heights where cloud top buoyancy estimates are unavailable.

Figure 6a shows the composite time series of $\overline{\hat{w}_c}$, implying the persistence of deep convection with the vertical velocity peak at 200–300 hPa. The near invariance of $\overline{\hat{w}_c}$ is not surprising, since the atmosphere stays humid and marginally unstable most of the time given that the statistics are constructed around the occurrence of organized convection over tropical oceans. Convection therefore has the potential to develop deep whenever it occurs, whereas the frequency of occurrence may be largely modulated by the large-scale dynamics as shown later. A closer examination, however, reveals a subtle but systematic variation in $\overline{\hat{w}_c}$. The atmosphere undergoes a gradual lower tropospheric moistening (destabilization) toward the time of convection and a subsequent near-surface cooling (stabilization) [*Masunaga*, 2012], which is probably responsible for a slight intensification during negative hours and a sudden weakening of $\overline{\hat{w}_c}$ at $t \sim 0$. It is noted that the persistence of deep convection could be somewhat exaggerated because less developed convection concealed beneath an overlapping high cloud would be difficult to sample from infrared measurements.

It is reminded that samples of convective clouds are absent when cloud top height does not reach beyond 3 km. It is attempted here to fill in the effects of shallow cumuli by a simplistic approach where the $\overline{\hat{w}_c}$ profile is prescribed with the most heavily entraining plume model simulation, plotted in darkest blue in Figure 2. This choice of the least-developed cumulus profile is intended to provide a conservative estimate of shallow convective updraft. The result emerges as a weak enhancement of $\overline{\hat{w}_c}$ below 3 km (hatched in Figure 6a), somewhat strengthening as the ambient atmosphere moistens toward time zero. Shallow cumulus

is nevertheless weak in the variability of $\overline{\hat{w}_c}$ as one might expect from its ubiquitous nature over tropical oceans [e.g., *Short and Nakamura*, 2000] and is hence unlikely to introduce significant error in the $\overline{\hat{w}_c}$ variability.

Convective mass flux (Figure 6b) has a bottom-heavy profile compared to $\overline{\hat{w}_c}$ as a result of the upward decreasing ρ. Another feature contrasting with $\overline{\hat{w}_c}$ is that $\overline{M_c}$ experiences a drastic enhancement during the hours of active convection. Convective mass flux reaches as large as $2-3\times10^{-2}$ kg m^{-2} s^{-1} at times when convection is most intense ($t \sim -3$ h), while an order of magnitude smaller during the hours away from the peak (hereafter called the background). This enhancement occurs in parallel with the sample size of convective clouds (solid curve in Figure 6c), which primarily reflects the frequency of convective occurrence since CloudSat overpasses are overall homogeneously sampled ($\sim4-5\times10^5$) along the composite time axis (dotted curve in Figure 6c). The number of convective cloud samples with buoyancy estimates spans the range from around 1000 in the background up to ~3000 at the peak convection, or from 0.2–0.25% to 0.6–0.75% when translated into the convective cloud cover, σ_c. Note that these values correspond to the coverage of convective cores that are selected by some rather strict criteria on radar echo characteristics, as described in [*Luo et al.*, 2010]; convective cores usually cover only a very tiny fraction of the whole convective cloud system. Equation (23) may be rewritten as $\overline{M_c} \sim \sigma_c \rho \overline{\hat{w}_c}$ when $\hat{w}_c$ is relatively constant throughout the evolution as is actually the case, so that $\overline{M_c}$ evolves roughly in proportional to σ_c. *Kumar et al.* [2015] also concluded based on their wind-profiler and radar measurements that the cumulus cloud cover, rather than vertical velocity, chiefly contributes to the variability of the domain-mean mass flux.

The third (green dashed) curve in Figure 6c provides a rough measure of shallow cumulus occurrence as defined by $N_{\mathrm{Cu}}^{2\mathrm{km}} - N_{\mathrm{Cu}}^{4\mathrm{km}}$, where N_{Cu} is the sample size of the cumulus (Cu) category at the indicated height from the CloudSat CLDCLASS product [*Wang and Sassen*, 2001]. The subtraction by $N_{\mathrm{Cu}}^{4\mathrm{km}}$ is meant to avoid congestus clouds already included in the buoyancy samples. The small sample size and weak updraft result in a barely visible contribution of shallow cumuli to convective mass flux (hatched in Figure 6b). Note that the CloudSat radar is insensitive to clouds whose droplets are too small to detect, and the shallow cumulus mass flux may be underestimated. This limitation is to be mitigated in future work using additional satellite instruments capable to detect thin low clouds such as CALIOP together with improved cloud-model setups that better characterize shallow cumuli.

Convective mass flux is next compared against an independent measurement of $\overline{\omega}$ as described in section 2.3. The total large-scale mass flux, $\overline{M_0}$, is proportional to $\overline{\omega}$ under the hydrostatic assumption and is broken down into three components;

$$\overline{M_0} \equiv \frac{\overline{\omega}}{g} = \overline{M_c} + \overline{M_R} + \overline{M_*}, \tag{24}$$

where $\overline{M_R}$ is the radiatively forced subsidence,

$$\overline{M_R}\frac{\partial \overline{s_a}}{\partial p} = \frac{\overline{Q_R}}{g}, \tag{25}$$

where s_a is DSE of the ambient air and Q_R is the radiative cooling rate adopted from the CloudSat 2B-FLXHR-LIDAR product. The last term, $\overline{M_*}$, is the residual mass flux unaccounted for by the other terms in the mass balance equation (24).

Figures 7a–7c show each mass flux component at different pressure levels of 200, 300, and 400 hPa. Convective mass flux delineates coherent evolutionary tracks across all the levels. The evolution of $\overline{M_0}$ begins with a weak ascent comparable to $\overline{M_c}$ but then rapidly grows to a striking updraft around time zero to a degree that $\overline{M_c}$ alone is far from able to account for. This discrepancy in the peak amplitude gives rise to a substantial magnitude of the residual flux $\overline{M_*}$, which at its maximum momentarily exceeds $\overline{M_c}$ at 400 hPa while staying relatively minor at 200 hPa. During the whole period, $\overline{M_R}$ is negligible and has little impact on the mass flux balance.

The vertical structure of $\overline{M_0}$ and $\overline{M_*}$ is presented in Figures 7d and 7e. As seen above, the most conspicuous feature in $\overline{M_*}$ is the upper tropospheric updraft peak around the hours of intense convection. Figure 7e shows that $\overline{M_*}$ is also characterized by a lower tropospheric downdraft persistent throughout the entire time series. The downdraft arises either when the total domain-mean ascent is short of the convective updraft or when $\overline{M_0}$ is negative in the first place. It is noted that the $\overline{M_*}$ downdraft occurs mostly at heights below 3 km (hatched), where the $\overline{M_c}$ updraft is likely to be underestimated because shallow cumuli are not fully considered in this

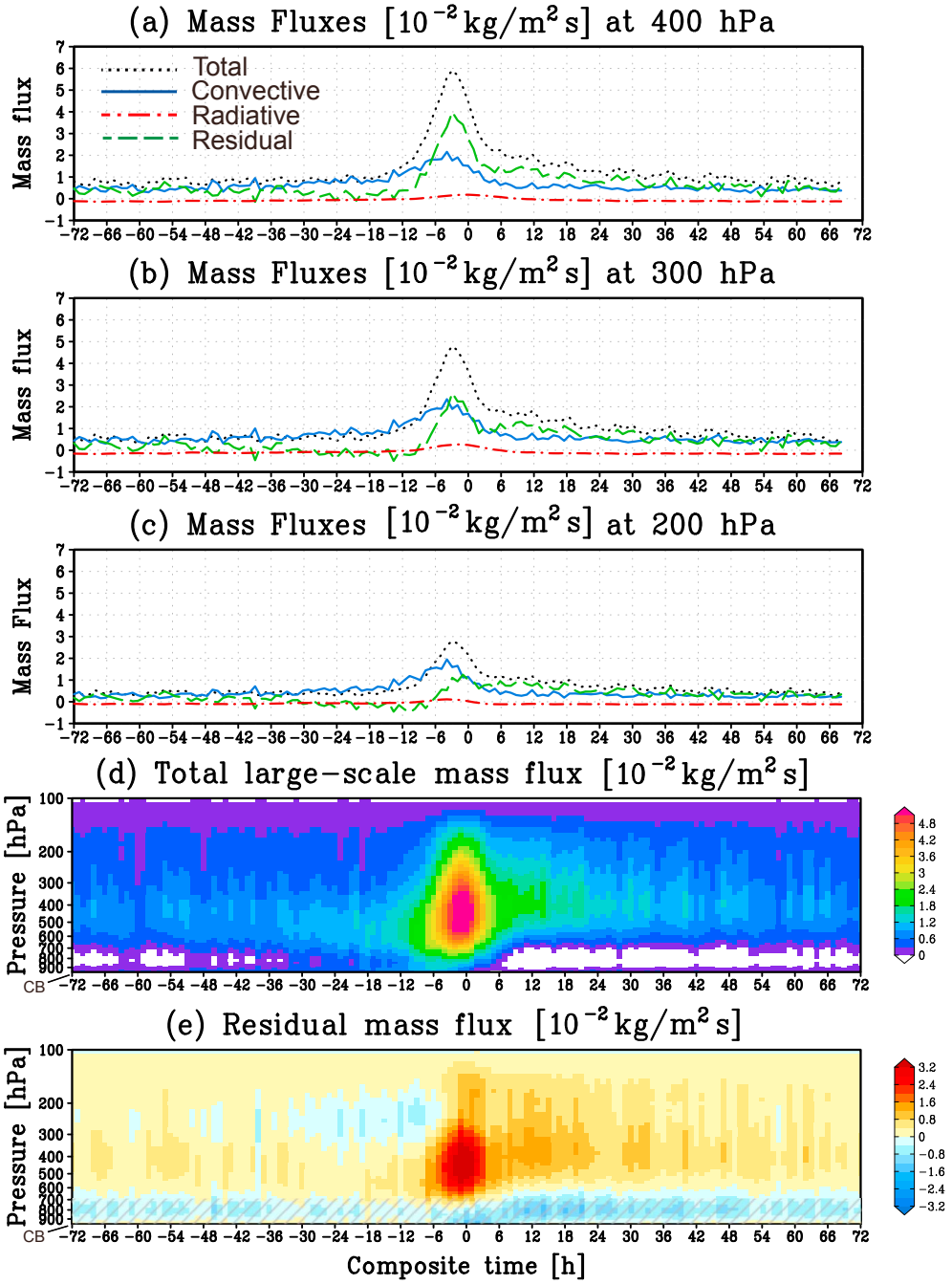

Figure 7. The composite time series of convective mass flux $\overline{M_c}$, total mass flux $\overline{M_0}$, radiatively forced mass flux $\overline{M_R}$, and residual mass flux $\overline{M_*}$ at (a) 400 hPa, (b) 300 hPa, and (c) 200 hPa. The complete vertical structure of (d) total mass flux $\overline{M_0}$ and (e) residual mass flux $\overline{M_*}$. The mass flux unit is 10^{-2} kg m^{-2} s^{-1}.

study. The $\overline{M_*}$ downdraft is hence probably underestimated as well because (24) needs to be satisfied for a given estimate of $\overline{M_0}$. Physical implications of the residual mass flux will be discussed in the next section.

5. Discussion and Conclusions

In this work, a new methodology is explored to derive the convective and total mass fluxes from a variety of satellite measurements. Convective-scale vertical velocity is profiled using cloud top (>3 km) buoyancy (or cloud top vertical velocity) estimates with the aid of a single-column plume model, while large-scale vertical motion is evaluated from a thermodynamic consideration applied to satellite soundings.

Both the convective- and large-scale vertical velocities are composited together into statistical time series constructed in association with the development and dissipation of organized convective systems.

In-cloud vertical velocity profiles are found to be peaked in the upper troposphere regardless of the evolutionary stage of convective development. It follows that deep convection in the relatively quiescent spells builds up, once it occurs, as vigorously (or even somewhat more intensively) as during organized systems. It is the frequency of convective occurrence rather than the individual cloud properties that modulates the convective mass flux as convective systems develop and dissipate, consistent with a recent study by *Kumar et al.* [2015] that used collocated wind-profiler and precipitation radar measurements. These findings are in harmony with existing observational work of the Madden-Julian Oscillation despite the vast difference in time scale, showing that deep convection prevails throughout although convection better structures itself into an organized system with extensive stratiform clouds during the mature phase than in the dry phase [*Morita et al.*, 2006; *Tromeur and Rossow*, 2010].

When the convective and total mass fluxes, $\overline{M_c}$ and $\overline{M_0}$, are compared, the mass balance relationship requires a residual mass flux, $\overline{M_*}$, that exhibits a significant updraft peak in the upper troposphere at the time of peak convection and a persistent lower tropospheric downdraft. The residual flux arises for several possible reasons. One possibility is retrieval bias since the measurements of $\overline{M_c}$ and $\overline{M_0}$ are derived in quite different manners and, therefore, would have independent sources of uncertainty that are hardly canceled out. An error analysis provided in Appendix A, however, suggests that the current estimate of $\overline{M_c}$ lies close to the higher end within the range of uncertainty examined, so that the residual flux is unlikely ascribed entirely to retrieval bias.

There are multiple lines of circumstantial evidence suggesting that $\overline{M_*}$ indeed embodies an actual physical entity, primarily ascribable to stratiform updraft and downdraft. First, $\overline{M_c}$ closely tracks $\overline{M_0}$ before convection begins to be invigorated and organized, leaving $\overline{M_*}$ stays near zero. This is as expected in that isolated convection is exclusively responsible for convective mass flux in the absence of organized convective systems. The high similarity between $\overline{M_c}$ and $\overline{M_0}$ except when convection is organized probably serves as indirect evidence that our estimations of $\overline{M_c}$ and $\overline{M_0}$, although obtained through entirely independent and separate channels, are rather unbiased. Second, the observed pair of upper tropospheric updraft and lower tropospheric downdraft in $\overline{M_*}$ is a known signature of stratiform dynamics (*Zipser* [1977] and *Houze* [1982], among others). Lastly, the known fact that stratiform updraft is most active during the mature and dissipating phases of organized convective systems conforms with the evolution of $\overline{M_*}$, which rapidly grows near time zero and subsequently fades away over time. Indeed, this temporal pattern of $\overline{M_*}$ qualitatively traces the variability of the second baroclinic (or stratiform) mode of large-scale vertical motion (Figure 5a of *Masunaga and L'Ecuyer* [2014]).

The algorithm requires technical refinements with particular focus on major outstanding issues including the crude assumptions on the plume model and shallow cumuli and the exclusion of continental convection. With this caveat, the current methodology is expected to open new pathways for a further understanding of tropical atmospheric dynamics. In particular, the present analysis of convective mass flux and total large-scale mass flux could be of unique utility for the observational diagnosis and evaluation of cumulus parameterizations in a global sense.

Appendix A: Error Analysis of Convective Mass Flux

A brief error analysis is provided in this section to demonstrate uncertainties in the composite time series of $\overline{M_c}$. The sources of errors examined here are the prescribed assumptions in the plume model as investigated in section 3.1 and the measurement errors (σ_z and σ_T) assumed for the Bayesian estimation (section 3.2). Other uncertainties related to cloud top buoyancy (section 2.2), large-scale mean vertical motion (section 2.3), and the composite satellite soundings (section 2.4) are discussed elsewhere [*Luo et al.*, 2010; *Masunaga*, 2012, 2013, 2015] and are not repeated here.

Figure A1 summarizes the error analysis results at three pressure levels. The assumptions being tested are a_B, $q_{w,\mathrm{crit}}$, and τ_{auto} from the plume model assumptions and σ_z and σ_T from the Bayesian estimation. Note that dT_i is not included because its uncertainty has little impact on the plume model solutions (Figures 4c and 4d). The sensitivity to the model assumptions is largest near the time of convective peak ($t \approx 0$) at all heights, with the magnitude decreasing with increasing height. Among the parameters examined, $q_{w,\mathrm{crit}}$ and τ_{auto} have the greatest contributions at 300 and 400 hPa. The amplitude of the σ_z and σ_T uncertainties remains small, although recognizable at 200 hPa. The control run stays close to the high end of the error range throughout the evolution particularly at 300 and 400 hPa. It follows that $\overline{M_c}$ is more likely overestimated than

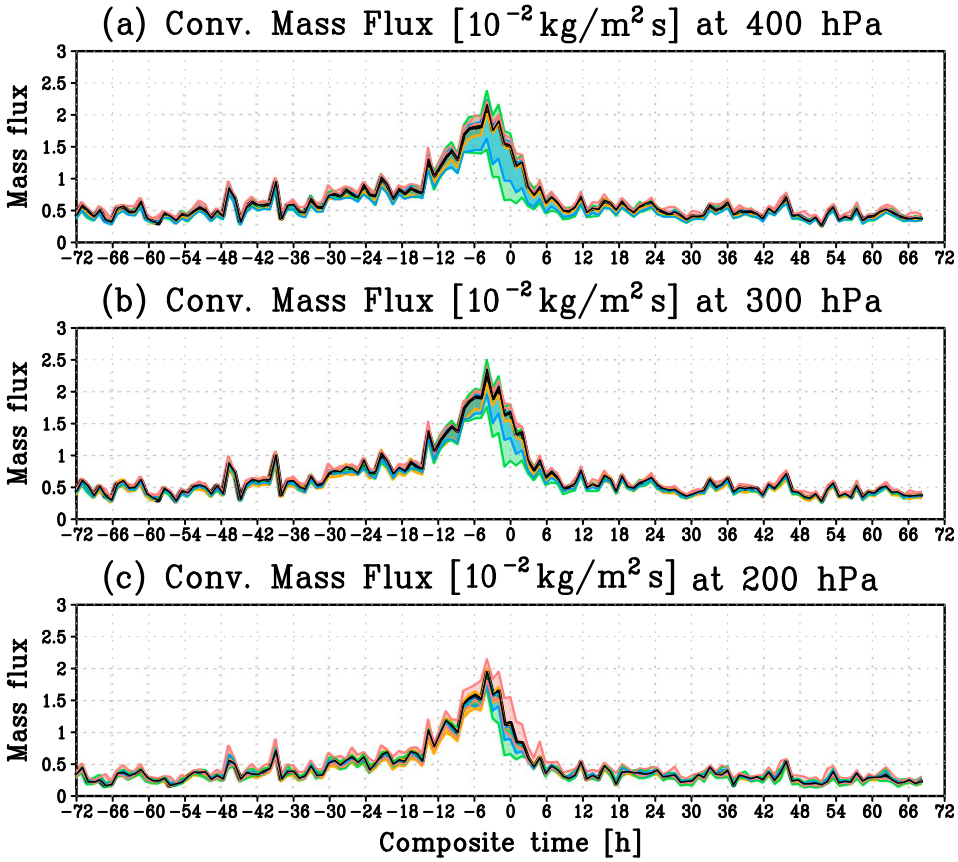

Figure A1. The composite time series of convective mass flux, $\overline{M_c}$, for a range of model assumptions and measurement errors at (a) 400 hPa, (b) 300 hPa, and (c) 200 hPa. The mass flux unit is 10^{-2} kg m^{-2} s^{-1}. The range of uncertainties is shaded in orange for a_B, blue for $q_{w,\mathrm{crit}}$, green for τ_{auto}, and red for the measurement error (σ_z and σ_T). The lower and upper ends of each model assumption are as indicated in Table 2. The measurement error range is bounded by (σ_z, σ_T) = (1.5 km, 1 K) and (0.5 km, 2 K). The control run, identical to the blue solid curve in Figures 7a–7c, is plotted in black.

underestimated in the present analysis, suggesting that the residual mass flux, $\overline{M_*}$, from the control run is plausibly a conservative estimate for given $\overline{M_0}$.

The drag of precipitation is not included and is difficult to quantify for uncertainty in the present model where precipitation immediately falls out and is not tracked down further. The absence of precipitation drag would lead to an overestimation of buoyancy and hence an underestimation of the residual mass flux. The upper tropospheric updraft in $\overline{M_*}$ thus could be even larger, while the lower tropospheric downdraft might have been somewhat exaggerated.

The error magnitude is minimal in the background state away from the hours of vigorous convection. It is implied that the earlier conclusion that $\overline{M_c}$ solely accounts for $\overline{M_0}$ before convection is invigorated remains robust regardless of prescribed assumptions.

References

Arakawa, A., and W. H. Schubert (1974), Interaction of a cumulus cloud ensemble with the large-scale environment. Part I., *J. Atmos. Sci.*, *31*, 674–701.

Asai, T., and A. Kasahara (1967), A theoretical study of the compensating downward motions associated with cumulus clouds, *J. Atmos. Sci.*, *24*, 487–496.

Deser, C. (1994), Daily surface wind variations over the equatorial Pacific Ocean, *J. Geophys. Res.*, *99*, 23,071–23,078.

Grant, A. L. M. (2001), Cloud-base fluxes in the cumulus-capped boundary layer, *Q. J. R. Meteorol. Soc.*, *127*, 407–421.

Gregory, D. (2001), Estimation of entrainment rate in simple models of convective clouds, *Q. J. R. Meteorol. Soc.*, *127*, 53–72.

Heymsfield, G. M., L. Tian, A. J. Heymsfield, L. Li, and S. Guimond (2010), Characteristics of deep tropical and subtropical convection from nadir-viewing high-altitude airborne Doppler radar, *J. Atmos. Sci.*, *67*, 285–308.

Houghton, H. G., and H. E. Cramer (1951), A theory of entrainment in convective currents, *J. Meteorol.*, *8*, 95–102.

Houze, R. A. J. (1982), Cloud clusters and large-scale vertical motions in the tropics, *J. Meteorol. Soc. Jpn.*, *60*, 396–410.

Acknowledgments
The authors are grateful to Bill Rossow and Kenta Suzuki for their comments on earlier versions of the manuscript. The AIRS/AMSU product was provided by Goddard Earth Sciences (GES) Data and Information Services Center (DISC) (http://disc.sci.gsfc.nasa.gov) and the TRMM PR (2A25) data set by the Japan Aerospace Exploration Agency (JAXA) (https://www.gportal.jaxa.jp/gp/top.html). The data sets also crucial, although not explicitly presented, in the current analysis are the GPROF 2010 precipitation product from Colorado State University (http://rain.atmos.colostate.edu/RAINMAP), the AMSR-E SST and CWV product by Remote Sensing Systems (http://www.remss.com), the CloudSat data sets by the CloudSat Data Processing Center (http://www.cloudsat.cira.colostate.edu), and QuikSCAT data from the NASA Jet Propulsion Laboratory (https://podaac.jpl.nasa.gov/QuikSCAT). H.M. is supported by the Japan Society for the Promotion of Science (JSPS) Grant-in-Aid (KAKENHI) for Challenging Exploratory Research (26610150). Z. J. L. would like to acknowledge funding support by NASA grant NNX12AC13G and support from JPL CloudSat and Radar Science and Engineering group.

Imaoka, K., and R. W. Spencer (2000), Diurnal variation of precipitation over the tropical oceans observed by TRMM/TMI combined with SSM/I, *J. Clim.*, *13*, 4149–4158.
Johnson, R. H., T. M. Rickenbach, S. A. Rutledge, P. E. Ciesielski, and W. H. Schubert (1999), Trimodal characteristics of tropical convection, *J. Clim.*, *12*, 2397–2418.
Kessler, E. (1969), *On the Distribution and Continuity of Water Substance in Atmospheric Circulations*, Am. Meteorol. Soc., pp. 1–84, Boston.
Kumar, V. V., C. Jakob, A. Protat, C. R. Williams, and P. T. May (2015), Mass-flux characteristics of tropical cumulus clouds from wind profiler observations at Darwin, Australia, *J. Atmos. Sci.*, *72*, 1837–1855, doi:10.1175/JAS-D-14-0259.1.
Kummerow, C. D., S. Ringerud, J. Crook, D. Randel, and W. Berg (2011), An observationally generated a-priori database for microwave rainfall retrievals, *28*, 113–130.
LeMone, M. A., and E. J. Zipser (1980), Cumulusnimbus vertical velocity events in GATE. Part I: Diameter, intensity and mass flux, *J. Atmos. Sci.*, *37*, 2444–2457.
Liu, C., E. J. Zipser, and S. W. Nesbitt (2007), Global distribution of tropical deep convection: Different perspectives from TRMM infrared and radar data, *J. Clim.*, *20*, 489–503.
Lorenc, A. C. (1986), Analysis methods for numerical weather prediction, *Q. J. R. Meteorol. Soc.*, *112*, 1177–1194.
Luo, Z. J., G. Y. Liu, and G. L. Stephens (2010), Use of A-Train data to estimate convective buoyancy and entrainment rate, *Geophys. Res. Lett.*, *37*, L09804, doi:10.1029/2010GL042904.
Luo, Z. J., J. Jeyaratnam, S. Iwasaki, H. Takahashi, and R. Anderson (2014), Convective vertical velocity and cloud internal vertical structure: An A-Train perspective, *Geophys. Res. Lett.*, *41*, 723–729, doi:10.1002/2013GL058922.
Masunaga, H. (2012), A satellite study of the atmospheric forcing and response to moist convection over tropical and subtropical oceans, *J. Atmos. Sci.*, *69*, 150–167.
Masunaga, H. (2013), A satellite study of tropical moist convection and environmental variability: A moisture and thermal budget analysis, *J. Atmos. Sci.*, *70*, 2443–2466.
Masunaga, H. (2015), Assessment of a satellite-based atmospheric budget analysis method using CINDY2011/DYNAMO/AMIE and TOGA COARE sounding array data, *J. Meteorol. Soc. Jpn*, *93A*, 21–40.
Masunaga, H., and T. S. L'Ecuyer (2014), A mechanism of tropical convection inferred from observed variability in the moist static energy budget, *J. Atmos. Sci.*, *71*, 3747–3766.
May, P. T., and D. K. Rajopathyaya (1999), Vertical velocity characteristics of deep convection over Darwin, Australia, *Mon. Weather Rev.*, *127*, 1056–1071.
Mohr, K. I., and E. J. Zipser (1996), Defining mesoscale convective systems by their 85 GHz ice-scattering signatures, *Bull. Am. Meteorol. Soc.*, *77*, 1179–1189.
Morita, J., Y. N. Takayabu, S. Shige, and Y. Kodama (2006), Analysis of rainfall characteristics of the Madden-Julian Oscillation using TRMM satellite data, *Dyn. Atmos. Oceans*, *42*, 107–126.
Perry, K. L. (2001), SeaWinds on QuikSCAT level 3 daily, gridded ocean wind vectors (JPL SeaWinds project) version 1.1, JPL document D-20335, Jet Propulsion Laboratory. [Available at ftp://podaac.jpl.nasa.gov/OceanWinds/quikscat/L3/jpl/v2/docs/qscat_L3.pdf.]
Short, D. A., and K. Nakamura (2000), TRMM radar observations of shallow precipitation over the tropical oceans, *J. Clim.*, *13*, 4107–4124.
Simpson, J., and V. Wiggert (1969), Models of precipitating cumulus towers, *Mon. Weather Rev.*, *97*, 471–489.
Susskind, J., C. D. Barnet, and J. M. Blaisdell (2003), Retrieval of atmospheric and surface parameters from AIRS/AMSU/HSB data in the presence of clouds, *IEEE Trans. Geosci. Remote Sens.*, *41*, 390–409.
Susskind, J., J. M. Blaisdell, L. Iredell, and F. Keita (2011), Improved temperature sounding and quality control methodology using AIRS/AMSU data: The AIRS science team version 5 retrieval algorithm, *IEEE Trans. Geosci. Remote Sens.*, *49*, 883–907.
Takahashi, H., and Z. J. Luo (2012), Where is the level of neutral buoyancy for deep convection?, *Geophys. Res. Lett.*, *39*, L15809, doi:10.1029/2012GL052638.
Tromeur, E., and W. B. Rossow (2010), Interaction of tropical deep convection with the large-scale circulation in the MJO, *J. Clim.*, *23*, 1837–1853.
Wang, C., Z. J. Luo, X. Cheng, X. Zeng, W.-K. Tao, and X. Huang (2014), A physically based algorithm for non-blackbody correction of cloud-top temperature and application to convection study, *J. Appl. Meteorol. Climatol.*, *53*, 1844–1857.
Wang, Z., and K. Sassen (2001), Cloud type and macrophysical property retrieval using multiple remote sensors, *J. Appl. Meteorol.*, *40*, 1665–1682.
Wentz, F. J., and T. Meissner (2000), *AMSR Ocean Algorithm, Algorithm Theoretical Basis Document*, Remote Sensing Systems, Santa Rosa, Calif. [Available at http://www.ssmi.com/.]
Yanai, M., S. Esbensen, and J.-H. Chu (1973), Determination of bulk properties of tropical cloud clusters from large scale heat and moisture budgets, *J. Atmos. Sci.*, *30*, 611–627.
Zipser, E. J. (1977), Mesoscale and convective-scale downdrafts as distinct components of squall-line structure, *Mon. Weather Rev.*, *105*, 1568–1589.
Zipser, E. J. (2003), Some views on "Hot Towers" after 50 years of tropical field programs and two years of TRMM data, in *Cloud Systems, Hurricanes, and the Tropical Rainfall Measuring Mission (TRMM), Meteor. Monogr.*, vol. 29, pp. 49–58, Am. Meteorol. Soc.